UC Davis
UC Davis Previously Published Works

Title

Detection of spatially distributed damage in fiber-reinforced polymer composites

Permalink

Journal

ISSN

Authors

Loyola, Bryan R
Briggs, Timothy M
Arronche, Luciana
et al.

Publication Date

DOI

Peer reviewed

Structural Health Monitoring

Detection of Spatially Distributed Damage in Fiber-Reinforced Polymer Composites

Journal:	*Structural Health Monitoring*
Manuscript ID:	SHM-12-0091.R1
Manuscript Type:	Original Manuscript
Date Submitted by the Author:	n/a
Complete List of Authors:	Loyola, Bryan; Univ of California, Davis, Mechanical & Aerospace Engineering Briggs, Timothy; Sandia National Laboratories, Arronche, Luciana; Univ of California, Davis, Mechanical & Aerospace Engineering Loh, Kenneth; Univ of California, Davis, Civil & Environmental Eng La Saponara, Valeria; Univ of California, Davis, Mechanical & Aerospace Engineering
Keywords:	carbon nanotube, electrical impedance tomography, fiber-reinforced polymer composite, impact damage detection, spatial conductivity mapping, strain sensing, structural health monitoring, thin film
Abstract:	This work describes a novel method of embedded damage detection within glass fiber reinforced polymer (GFRP) composites. Damage detection is achieved by monitoring the spatially-distributed electrical conductivity of a strain sensitive multi-walled carbon nanotube (MWCNT) thin film. First, thin films were spray-deposited directly upon glass fiber mats. Second, using electrical impedance tomography (EIT), the spatial conductivity distribution of the thin film was determined before and after damage-inducing events. The resolution of the sensor was determined by drilling progressively larger holes in the center of the composite specimens, and the corresponding EIT response was measured by recording the current-voltage data at the periphery of the monitored composite sample. In addition, the sensitivity to damage occurring at different locations in the composite was also investigated by comparing EIT spatial conductivity maps obtained for specimens with sets of holes drilled at different locations in the sensing area. Finally, the location and severity of damage from low velocity impact events was detected using the EIT method. The work presented in this study indicates a paradigm shift in the available possibilities for structural health monitoring of fiber-reinforced polymer composites.

1
2
3
4
5
6
7
8
9
10
11
12
13
14
15
16
17
18
19
20
21
22
23
24
25
26
27
28
29
30
31
32
33
34
35
36
37
38
39
40
41
42
43
44
45
46
47
48
49
50
51
52
53
54
55
56
57
58
59
60

Detection of Spatially Distributed Damage in Fiber-Reinforced Polymer Composites

Bryan R. Loyola[1,2], Timothy M. Briggs[2], Luciana Arronche[1], Kenneth J. Loh[3,], Valeria La Saponara[1,§], Greg O'Bryan[2], and Jack L. Skinner[2,4]

[1]Department of Mechanical and Aerospace Engineering, University of California, Davis, CA 95616, USA
[2]Sandia National Laboratories, Livermore, CA 94550, USA
[3]Department of Civil and Environmental Engineering, University of California, Davis, CA 95616, USA
[4]Department of General Engineering, Montana Tech, Butte, MT 59701, USA
e-mail: kjloh@ucdavis.edu
[§]e-mail: vlasaponara@ucdavis.edu

This work describes a novel method of embedded damage detection within glass fiber reinforced polymer (GFRP) composites. Damage detection is achieved by monitoring the spatially-distributed electrical conductivity of a strain sensitive multi-walled carbon nanotube (MWCNT) thin film. First, thin films were spray-deposited directly upon glass fiber mats. Second, using electrical impedance tomography (EIT), the spatial conductivity distribution of the thin film was determined before and after damage-inducing events. The resolution of the sensor was determined by drilling progressively larger holes in the center of the composite specimens, and the corresponding EIT response was measured by recording the current-voltage data at the periphery of the monitored composite sample. In addition, the sensitivity to damage occurring at different locations in the composite was also investigated by comparing EIT spatial conductivity maps obtained for specimens with sets of holes drilled at different locations in the sensing area. Finally, the location and severity of damage from low velocity impact events was detected using the EIT method. The work presented in this study indicates a paradigm shift in the available possibilities for structural health monitoring of fiber-reinforced polymer composites.

1. Introduction

For over 50 years, fiber-reinforced polymer (FRP) composites have been used with increasing frequency in retrofitted and newly fabricated structures. This utilization spans the aerospace, wind turbine, automotive, naval, and civil industries. The reason for their widespread adoption is that FRPs feature high strength-to-weight ratios, resistance to fatigue and corrosion, as well as high conformability and tailorability to efficiently meet design allowables. Despite these impressive characteristics, FRPs are still susceptible to damage due to a variety of scenarios, including overloading, impact events, chemical penetration, multi-axial fatigue, or a combination of any/all of the above. Such damage tends to manifest in various modes, such as delamination, fiber- or matrix-fracture, fiber-matrix debonding, and matrix swelling. Damage typically occurs subsurface within the laminate architecture of the composite, thereby making damage barely visible to inspectors. As visual inspection is a common structural monitoring approach [1, 2], the possibility of unseen damage growing to critical levels without detection is a serious cause for concern.

Due to the internal nature of damage within FRP composites, several groups have focused on embedding sensing methodologies into the layered architecture of a composite stack sequence. Direct strain measurements have been performed using embedded foil-based strain gages [3, 4] and fiber-Bragg gratings [5-8]. These are both point-based methodologies that have high resolution localized to the sensor position. However, to get a global view of structural health, dense instrumentation and interpolation methods must be implemented for damage detection purposes. It has also been found that an embedded optical fiber that has a diameter larger than 100 μm can lead to mechanical performance degradation [6]. Other groups have focused on embedding piezoelectric sensors within the composite architecture for acoustic

emission detection [9, 10] and ultrasonic imaging [11-13]. Acoustic emissions and ultrasonic imaging allow for higher resolution damage detection within the composite, but the presence of embedded piezoelectric sensors and actuators cause a localized stress concentration and can initiate a crack, thus leading to a shorter service life of the composite part [14].

To negate the issues of embedding macro-scale sensors within composite structures prone to complex damage at the micromechanics level, others have used changes in inherent or incorporated electrical properties of FRP composites for structural health monitoring (SHM). Several groups have measured the change in resistance of the fibers in carbon fiber-reinforced polymer (CFRP) composites while they are subjected to tensile and compressive loads [15-18]. In addition to characterizing CFRP strain sensitivity, others have characterized changes in their electrical properties due to incurred damage as a result of transverse cracking [19-21], fatigue loading [22], and delamination [23].

For non-conductive FRPs like glass-fiber reinforced polymer (GFRP) composites, carbon nanotube (CNT)-based nanocomposites have been investigated for *in situ* sensing. This work has been motivated by observing the high piezoresistivity of individual carbon nanotubes [24-26]; since this discovery, extensive work has been conducted in characterizing how electrical changes to these nanocomposites correlate to applied strain and resulting damage. Much of this work involves incorporating CNTs into the epoxy matrix of GFRPs. CNTs have been shown to not only enhance the mechanical properties of GFRPs but also introduce enhanced electrical conductivity to the epoxy matrix (*i.e.*, if the appropriate functionalization of CNTs are performed prior to their dispersion) [27-32]. Additional work has demonstrated the sensitivity of these epoxy-based nanocomposites to applied strain [33, 34] and damage [33-36]. Investigators have considered using CNT-based thin films for applied sensing. Typically, most work in this area

involves manufacturing a thin film and affixing it onto the structural surface to be monitored. In one case, the CNT-based thin film was deposited directly onto a glass fiber weave and embedded within a composite structure for actual *in situ* monitoring [37]. Unlike conventional point-based strain transducers, CNT-based thin films are sensitive to strain at every location of the film and where they have been applied throughout the structure. As long as a corresponding spatially-distributed electrical measurement method is available, the inherently distributed strain sensitivity of CNT-doped composites provides insight into both the location and magnitude of induced damage.

For just over 30 years, medical- and geophysical-focused research groups have been investigating the application of a soft-tomographic imaging method called electrical impedance tomography (EIT). EIT is capable of determining the conductivity distribution within a 2D or 3D body bounded by electrodes. An EIT measurement is taken by injecting current between two electrodes while simultaneously measuring the electric potential at the remaining electrodes. A full measurement consists of several of these electrical current injection-potential measurement patterns. The spatial conductivity distribution reconstruction is ill-posed, and its calculation has only been possible since the establishment of the mathematical framework proposed by Calderon [38] in 1980. Since then, several groups have created algorithms to perform this reconstruction using one-step [39, 40] or iterative [41-43] solvers for isotropic [44, 45] and anisotropic [46, 47] conductivity distributions. Very limited research has been conducted to date to adapt this electrical imaging modality to SHM applications; examples include work by Loh *et al.* [48] for strain/impact, Hou *et al.* [49] for pH, Pyo *et al.*[50] for corrosion, Lazarovitch *et al.* [51] for cracking, and Alirezaei *et al.* [52, 53] for pressure/deformation monitoring. Despite creating a

foundation for future EIT work in SHM, more studies are required to achieve embedded *in situ* sensing and to detect structural damage occurring within the material body.

This study introduces embedded spatial sensing for SHM of structural components such as FRPs. First, a strain sensitive multi-walled carbon nanotube (MWCNT)-poly(vinylidene fluoride) (PVDF) film is spray-deposited directly onto a glass fiber mat, which is then embedded in a GFRP composite. Depositing the MWCNT-PVDF thin film on the fiber mat allows for a higher sensitivity to fiber damage, and the film is protected from ambient environmental conditions by the encapsulating epoxy matrix. Second, EIT measurements are taken to detect damage from drilled holes, which represent well-defined damage. Once the sensitivity and resolution are established, EIT measurements are performed to detect damage from a range of low velocity impact energies. EIT takes advantage of the enhanced spatial strain sensitivity provided via MWCNT-PVDF thin-films by reconstructing its spatial conductivity distribution in which a change in electrical conductivity at each point is calibrated to the applied strain. The reconstructed spatial conductivity map thus provides location and magnitude information of damage. Finally, difficulties in measurement strategy and theoretical reconstruction arising from the specimens' anisotropic electrical conductivity (inherent with the unidirectional glass fiber mats used) have been overcome. This work establishes a foundation to enable a field-deployable *in situ* spatial damage detection methodology for GFRP composites.

2. Electrical Impedance Tomography

EIT is a soft-field tomographic imaging method that uses boundary voltage measurements from propagated electric current to reconstruct the 2D or 3D conductivity distribution with an area or volume bounded by measurement electrodes. A measurement is performed by injecting a current between two boundary electrodes, and the differential voltage is

measured for the remaining adjacent electrodes. To reduce electrode contact resistance effects, voltage measurements are not taken for the pair of electrodes used to inject current (where one is the input and another is set to ground). This approach allows for a more stable calculation of the voltage distribution for each current propagation [45]. The reconstruction of the conductivity distribution is based on Laplace's equation:

$$\nabla \cdot (\sigma \cdot \nabla u) = 0 \tag{1}$$

In Equation (1), σ represents the scalar conductivity distribution in the sensing area, and u is the corresponding voltage distribution, where both can be expressed as functions of spatial Cartesian coordinates in two and three dimensional space. Because very few analytical solutions are known for Equation 1, it is typical to perform these calculations numerically using the finite element method (FEM). The 2D conductive area is discretized into three-node triangular elements, where each element (n) has a scalar conductivity value of σ_n. In this study, each element is assumed to have a uniform conductivity. The numerical calculation is performed using a weak formulation of Laplace's equation described as:

$$\iint_{\Omega_n} \nabla \phi \cdot \sigma_n \cdot \nabla u \cdot dx dy = 0 \tag{2}$$

In Equation (2), ϕ is the linear shape function used to account for the voltage at each node. To model the current injection and ground boundary conditions, Equations (3) and (4) are applied at each electrode in the mesh:

$$\int_{E_l} \sigma_n \frac{\partial u}{\partial v} \cdot ds = I_l \ \text{for all elements along } E_l \tag{3}$$

$$u + z_l \cdot \sigma_n \cdot \frac{\partial u}{\partial v} = V_l \ \text{for all elements along } E_l \tag{4}$$

Equation (3) requires that the current injected at a specific electrode (E_l) must be normal to the surface of the electrodes and total the amount of current in the actual measurement. Equation (4) governs the voltage drop between the electrode and along the conductive medium due to contact resistance (z_l) [44, 54].

Typically, Laplace's equation is solved as a forward problem, where the body's conductivity distribution is known, and the boundary voltage distribution is calculated. In the case of EIT, the spatial conductivity is desired, whereas the boundary voltage values are known (*i.e.*, from experimental measurements), thus necessitating the solution of the inverse problem. As discussed previously, many reconstruction methods have been created in the literature. For SHM, detecting changes in the conductivity with respect to a baseline is needed for damage detection. For this reason, the linearized reconstruction strategy developed by Adler and Guardo [40] is used for normalized differential reconstruction. Their reconstruction algorithm, called Maximum a Posteriori (MAP), is a one-step solver, which is ideal for real-time measurements. For this reconstruction, two sets of boundary electrode voltage measurements are required, where an initial measurement is obtained and then compared to a measurement later in time. The difference is calculated for each individual voltage measurement (ΔV) and is then divided by the corresponding initial measurement (V_0). The reconstruction is based on:

$$\left\{\frac{\Delta\sigma}{\sigma_0}\right\} = \left[\left(H^T W H + \lambda R\right)^{-1} H^T W\right]\left\{\frac{\Delta V}{V_0}\right\}$$

(5)

The MAP algorithm reconstructs the normalized difference conductivity vector $\{\Delta\sigma/\sigma\}$ and is comprised of the normalized change in conductivity for each element (n) in the mesh using all of the normalized differential voltage measurements between two points in time. This reconstruction in Equation (5) is mainly governed by the sensitivity matrix (H), which correlates

a small, normalized change in conductivity in one element to a normalized change in voltage at the boundary electrodes. The sensitivity matrix takes changes from all of the elements into account, facilitating the reconstruction. Normalized differential imaging has the advantage that the injection current magnitude and the contact resistance values do not play a part in the calculation of the sensitivity matrix. The Gaussian white noise from the voltage measurements is taken into account in the variance matrix (W), where:

$$W_{i,i} = \frac{1}{\alpha_i}$$

(6)

In Equation (6), α_i is the variance for the ith measurement. As mentioned earlier, the EIT reconstruction is ill-posed due to the higher number of elements to reconstruct than the available voltage measurements.

The ill-posedness of the inverse problem is overcome through regularization, which typically imposes conditions of smoothness to stabilize the reconstruction. In this case, the regularization matrix (R) is based on a Gaussian high-pass filter to implement smoothing. The regularization hyperparameter (λ) must be determined to specify how much smoothing is necessary. This is accomplished by calculating the conductivity reconstructions corresponding to different λ values until the signal-to-noise ratio (SNR) is a specified multiple of the SNR of the voltage measurements. The ratio of the voltage SNR (SNR_V) to the SNR of the reconstructed conductivity (SNR_σ) is termed the noise figure (NF):

$$NF = \frac{SNR_V}{SNR_\sigma}$$

(7)

The NF used in this work has been set to 1, following the example of Graham and Adler [55]. A value of 1 is used to prevent over-smoothing of the reconstruction by mandating that the SNR_σ of the reconstruction is the same as SNR_V of the collected data.

3. Experimental Methodology

To demonstrate the performance of EIT as an embedded SHM methodology, a conductive and strain sensitive film needs to be deposited within the electrically non-conductive GFRP structure. A MWCNT-PVDF film was formulated and spray-deposited on a glass fiber mat, which was stacked with other glass fiber mats and infused with epoxy to fabricate GFRP panels. These specimens were characterized for their damage resolution using progressively larger diameter holes drilled in the center of the sensing area. In addition, sensitivity to damage occurring at different locations across the sensing area was also explored. Once the damage sensitivity was determined, the impact damage detection capability of the EIT method was investigated.

3.1 MWCNT-PVDF Film Fabrication

A two-part conductive film was formulated for spray-deposition over large substrates. The first component of the film formulation was based on an MWCNT-PSS/NMP solution. The formulation started with preparation of a 2 *wt.*% solution of poly(sodium 4-styrenesulfonate) (PSS) (~1M M_W, Sigma-Aldrich) that was dissolved in deionized (DI) water using high-energy tip-sonication (D-450D, Branson) for a minimum of 10 min. An appropriate amount of MWCNTs (SouthWest NanoTechnologies) and a polar solvent called N-methyl-2-pyrrolidone (NMP) (Sigma-Aldrich) was mixed and added to the PSS solution. The NMP was used as a coalescing agent for the PVDF particles, as will be discussed later. This MWCNT-PSS/NMP solution was tip-sonicated for 30 min in an ice bath, which was enough time to fully disperse the nanotubes. Dispersion was achieved via steric stabilization between the PSS and the MWCNTs [56]; the NMP also aided with the dispersal of the MWCNTs [57].
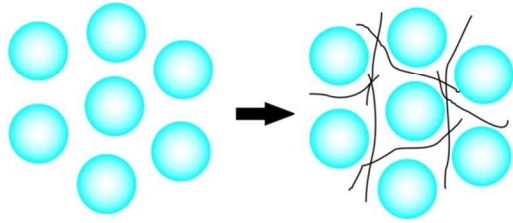
Figure 1. An illustration of the MWCNTs (black lines) in the PVDF (blue spheres) latex solution is shown.
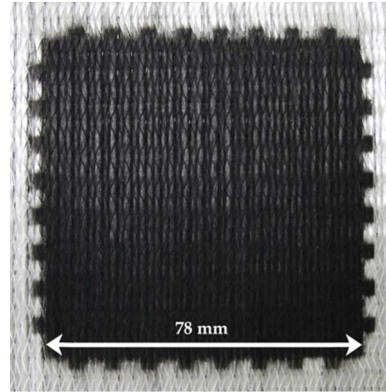

Figure 2. A photograph of the mask for one typical sensing area is shown. The smaller squares along film boundaries are contact locations for the electrode pads.

The second component of the formulation contained a latex of 150 nm-diameter spherical particles of Kynar PVDF suspended in an Aquatec surfactant solution (Arkema). The solution was diluted to an appropriate mass concentration using DI water. Just before spray-deposition, the first component was mixed vigorously into the second component. This created a segregated network of MWCNTs that were unable to penetrate the PVDF particles. The final solution prior to spray-deposition was 14% solids weight content with 5 *wt.*% MWCNTs. Figure 1 shows an illustration of this segregated network of MWCNTs in the latex solution.

Once the film formulation was fully incorporated, it was spray-deposited using a Paasche VL-series airbrush. The substrates, upon which the solutions were sprayed, were unidirectional E-LR 0908 fiber mats (Vectorply) cut to 381×381 mm^2. The substrates were masked to contain six equally spaced 78×78 mm^2 sensing areas. In addition, the mask also allowed one to spray eight 3×3 mm^2 squares along each side of the square sensing area. The squares along the film boundaries were used for the electrode pads and were separated 6 mm apart. Once the film was spray-deposited, the substrates were dried in an oven at 60 °C for 10 min. A representative dried film on a unidirectional glass fiber mat is displayed in Figure 2, in which one can see the electrode pads extending from the main sensing area.
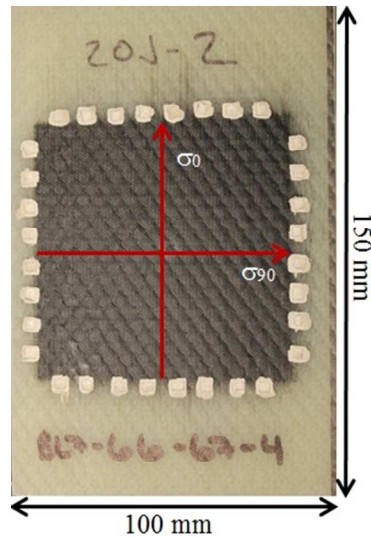
Figure 3. Photograph of a GFRP specimen with embedded MWCNT-PVDF film. The anisotropic nature of the conductivity is indicated by the arrows.

3.2 GFRP Composite Manufacturing

Once the MWCNT-PVDF film was deposited on a number of glass fiber mats, the GFRP composites were laid up in a $[0°/+45°/90°/-45°]_{2s}$ stack sequence, for a total of 16 layers. Using a vacuum-assisted resin transfer molding (VARTM) process, the stacked glass fiber mats were infused with a two-part epoxy system (117LV/237, Pro-Set), which was cured at 27 °C for 15 h and then 80 °C for 8 h. After completing the cure process, the panels were cut (with a diamond abrasive wet saw) into six $150×100$ mm^2 specimens as shown in Figure 3.

In order to allow for easy access to the sensing layers, the glass fiber mats with the applied MWCNT-PVDF films were only placed to be the top and bottom plies of the composite laminate with the films facing out. Since epoxy is nonconductive, easy access to the electrodes was facilitated prior to the infusion and curing of the epoxy. Here, adhesive copper tape, with a wax paper backing, was applied copper side down on each electrode pad of the MWCNT-PVDF film (prior to infusion) (Figure 4a). The tape was affixed using conductive colloidal silver paint (Ted Pella). After infusion, epoxy flowed around the applied copper tape and adhered to it

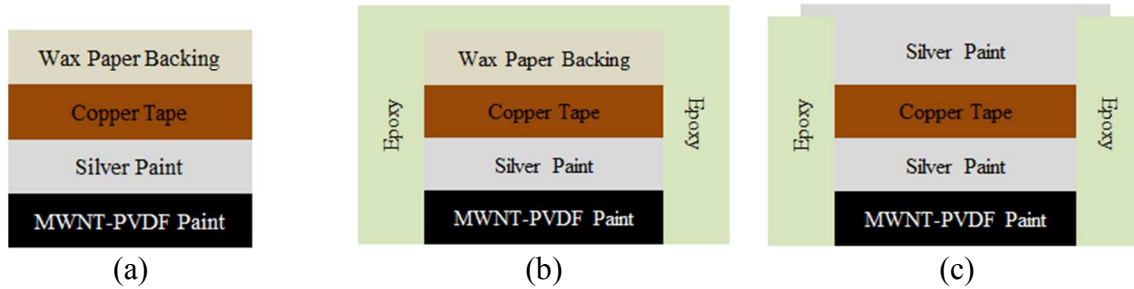<p style="text-align:center">(a)   (b)   (c)</p>

Figure 4. This schematic shows an exaggerated layout of the procedure for the electrode pad placement.

instead of the MWCNT-PVDF film of the electrode pad (Figure 4b). A razor blade was used to cut around the perimeter of the wax paper tape backing. The wax paper then detached from the conductive adhesive of the copper tape, and the tip of the knife was used to peel back the wax paper with encasing epoxy attached. To guarantee a good electrical connection, a top coat of colloidal silver paint was also applied to each exposed electrode (Figure 4c). The conductive electrode pad was then exposed and was used for performing the EIT measurements. Final preparation of each specimen involved uncovering all 32 electrodes.

3.3 Anisotropic Spatial Conductivity Considerations

Due to the stacking sequence, the outer plies had a fiber orientation of 0° direction, which lies in the vertical direction as shown in Figure 3. As a result, the conductivities in the vertical direction are approximately twice that of the horizontal direction. To accommodate this anisotropic conductivity, the scalar conductivity values in Equations (1-4) became matrix values with non-zero diagonal components. Therefore, the conductivity for each element can then be expressed as:

$$\sigma_n = \begin{bmatrix} \sigma_n^{90°} & 0 \\ 0 & \sigma_n^{0°} \end{bmatrix} = \begin{bmatrix} 1 & 0 \\ 0 & \left(\dfrac{\sigma^{0°}}{\sigma^{90°}}\right) \end{bmatrix} \sigma_n^{90°} = \begin{bmatrix} 1 & 0 \\ 0 & \left(\dfrac{\sigma^{0°}}{\sigma^{90°}}\right) \end{bmatrix} \sigma_n^* \qquad (8)$$
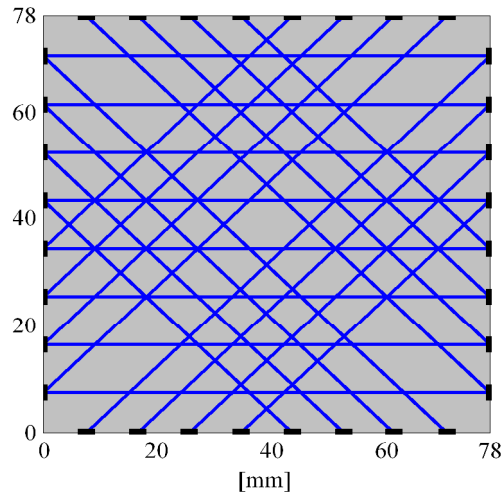
Figure 5. This schematic shows the current injection pattern used due to the anisotropic conductivity of the embedded MWCNT-PVDF films. The blue lines indicate current injection pairs, and the thick black lines along the boundaries are the electrodes.

The ratio of the directionally dependent conductivity values of $\sigma^{0°}$ and $\sigma^{90°}$ for the vertical and horizontal directions, respectively, were assumed to be the same for each element and determined by taking two-point probe resistance measurements across the sensing area, via the applied electrodes and in the directions indicated.

In the normalized differential reconstruction, only the scalar values of σ_n^{*} was reconstructed and not the full matrix. The degree of anisotropy was assumed to be the same across the sensing area, with the scalar value of the conductivity (σ_n^{*}) allowed to vary. This approach had been used before for other anisotropic EIT conductivity mapping applications [46, 47]. Introduction of the anisotropic conductivity into the sensitivity matrix was straightforward, where the conductivity matrix was directly applied to Equations (2-4) [47]. The anisotropic conductivity changed the EIT approach in two ways, which were the calculation of the sensitivity matrix and the pattern with which the current was injected. Figure 5 illustrates the current injection pattern used in this study, where the blue lines connect the injection-ground
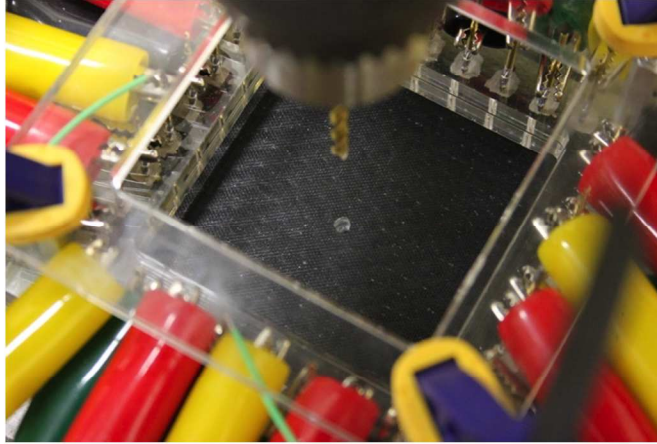
Figure 6. A customized fixture is used for obtaining EIT measurements. The image also shows a specimen undergoing the damage sensitivity characterization study after a 3.18 mm diameter hole has just been drilled.

electrode pairs. As indicated in Figure 5, electrical current is directed to flow transverse and diagonal to the vertical direction due to the anisotropic nature of spatial conductivity. If current is propagated in the vertical direction, the current distribution does not spread transverse to the current path, which leads to differential voltages of zero at the boundaries.

3.4 EIT Data Acquisition

As mentioned in Section 2, sets of current injection-boundary voltage measurements were required for solving the EIT inverse problem. A customized acrylic fixture with 32 spring-loaded pins was designed for interrogating the test specimens (Figure 6). The acrylic fixture was designed to fit directly over each composite specimen, and each of the spring-loaded pins was aligned with the corresponding film boundary electrode. The pins were positioned such that each contact head landed nominally at the center of the corresponding electrode. Boundary voltage measurements were collected using an Agilent 34980A multifunction switch/measure unit equipped with a 34932A matrix switch. A Keithley 6221 AC/DC current source was also connected to the Agilent 34980A switch for current generation and grounding. The current amplitude used in this study was a 100 μA DC current.
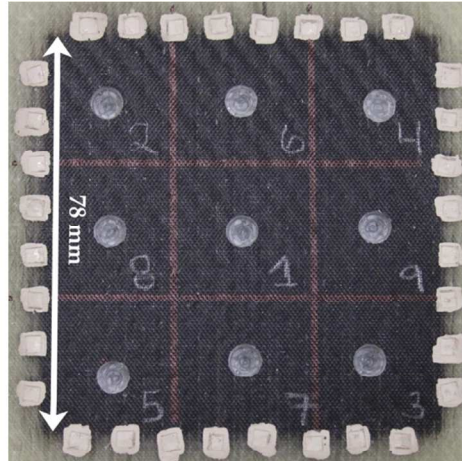
Figure 7. A representative specimen used for the damage sensitivity study is shown. A total of nine 6.35 mm holes have been drilled.

3.4 Damage Sensitivity Characterization

Progressively larger holes were drilled in the center of GFRP specimens for determining the damage detection resolution and sensitivity limit of the EIT method (Figure 6). The specimens were secured and mounted in a drill press while connected to the EIT measurement setup. Using titanium nitride-coated bits, holes of varying diameter (1.59 mm, 3.18 mm, 4.76 mm, 6.35 mm, 7.94 mm, 9.53 mm, and 12.7 mm) were drilled at the center of each specimen. An EIT measurement was taken before and after each hole was drilled. The EIT spatial conductivity reconstructions were performed in reference to the pristine pre-hole specimen.

In addition to characterizing the damage severity at the center of the sensing area, the sensitivity of EIT to damage occurring at different locations within the sensing area was also characterized. To perform this characterization, a 3×3 grid was drawn on a specimen as shown in Figure 7. In the center of each region, a 6.35 mm hole was drilled; the sequence of drilling was based on the numbers shown in Figure 7 (starting with the center). An EIT measurement was performed of the pristine specimen and after every hole was drilled. Once again, the EIT spatial conductivity images were reconstructed in reference to the pristine specimen.

3.5 Impact Damage Detection

With the sensitivity to prescribed damage sizes characterized, the proposed EIT technique was also investigated for detecting different magnitudes of impact damage. Following the ASTM standard D7136, specimens were subjected to nominal values of 20 J, 60 J, 100 J, and 140 J incident impact energies, using an instrumented Instron Dynatup 9250G drop-weight tester. The specimens were impacted with free-free boundary conditions using a 38.1 mm diameter hemispherical tup. EIT measurements were taken before and after each impact event. The reconstructions were conducted in reference to the initial measurement of the undamaged specimen. To verify the EIT response, the specimens were compared to photographs taken after the impact events.

4. Results and Discussion

4.1 Hyperparameter Calibration

As has been discussed in Section 2, a regularization hyperparameter must be determined for smoothing and stabilizing the EIT inverse problem. To find this parameter, a 6.35 mm hole has been drilled in the center of a pristine specimen as shown in Figure 8. EIT boundary electrode measurements have been acquired before and after drilling. Then, EIT spatial conductivity reconstructions have been performed using the two datasets and with varying hyperparameter values ranging from 10^2 to 10^{10}. For each reconstruction, the noise figure has been calculated using Equation (7), and the results are plotted in Figure 9. Using linear interpolation, the hyperparameter that corresponds to a *NF* of 1 has been determined and used for the remainder of this study.
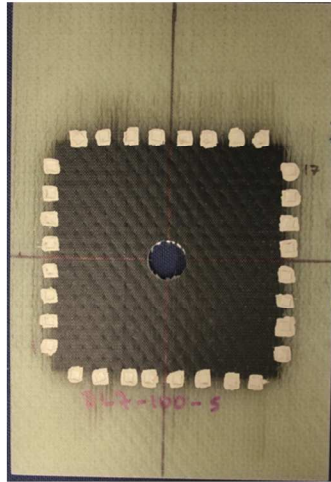
Figure 8. A GFRP specimen is shown with a 6.35 mm hole drilled in the center. This specimen was used to determine the hyperparameter.
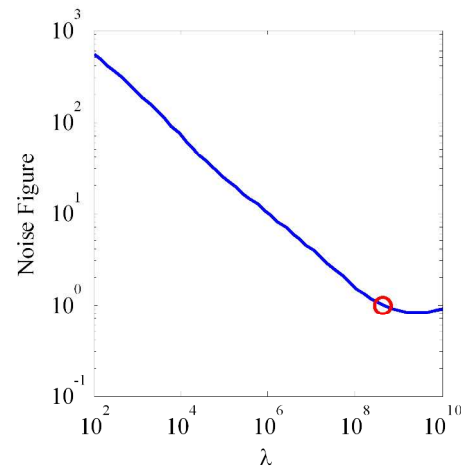
Figure 9. Noise figure is determined and plotted for values of hyperparameters ranging from 10^2 and 10^{10}. The hyperparameter with a *NF* of 1 is indicated with a red circle and has a value of $\lambda = 4.539 \times 10^8$.

The EIT reconstruction that corresponds to the hyperparameter with a *NF* of 1 is shown as a red circle in Figure 9. First, as described in Section 2, the EIT algorithm employed in this study solves for the relative or normalized change in spatial conductivity (Equation 5). Thus, the EIT spatial conductivity maps only show relative conductivity changes, where the normalized change in conductivity of each element in the EIT FEM model ($\Delta\sigma_N$) is defined as:

$$\Delta\sigma_N = \frac{\Delta\sigma}{\sigma_0} \cdot 100\%$$

(9)

Figure 10 shows the EIT spatial conductivity map for the drilled specimen shown in Figure 8. The decrease in conductivity that corresponds to the drilled hole can be easily discerned in the center of the sensing area. One aspect of this reconstruction is the positive change of conductivity that is collocated near the circumference of the drilled hole. This phenomenon tends to happen with many EIT reconstruction algorithms, where a sharp change in conductivity will cause the reconstruction to slightly trend towards the opposite magnitude (faint
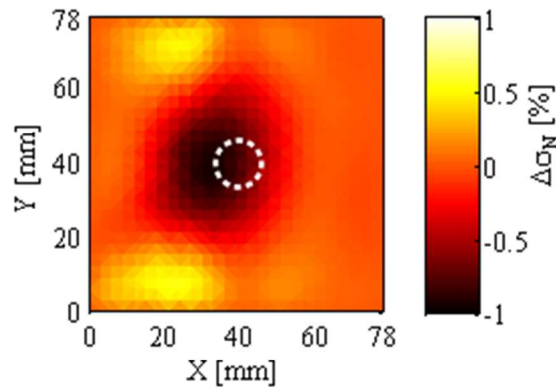
Figure 10. The EIT normalized spatial conductivity map for the specimen with a 6.35 mm center hole is shown. This reconstruction uses the hyperparameter that yielded a *NF* of 1. The dashed white circle indicates the locations of the actual hole.

yellow ring) before converging again to the actual conductivity distribution in the vicinity [40, 47, 55]. The two circular areas, one on the top-left and one on the bottom-left in Figure 10, are likely due to this phenomenon.

4.2 Damage Sensitivity Characterization

EIT damage sensitivity characterization studies based on the procedure outlined in Section 3.4 have been performed. EIT spatial conductivity maps corresponding to variations in drill-hole sizes and lateral hole placement have been reconstructed using the hyperparameter determined in Section 4.1. This study allows one to characterize the method's damage detection resolution and the sensitivity to damage located at different positions within the sensing area.

First, a set of representative EIT reconstructions corresponding to a specimen subjected to different drill-hole sizes is shown in Figure 11. From Figure 11b, one can see that damage due to a 3.18 mm diameter drilled hole is detectable, although the normalized change in conductivity is comparable to the level of background noise. This contrast continues to grow with increasing hole sizes, resulting in a contrast of about -1,000% for the 12.7 mm hole. While the theoretical normalized decrease in conductivity (Equation 9) is -100%, it is thought that the exaggeration
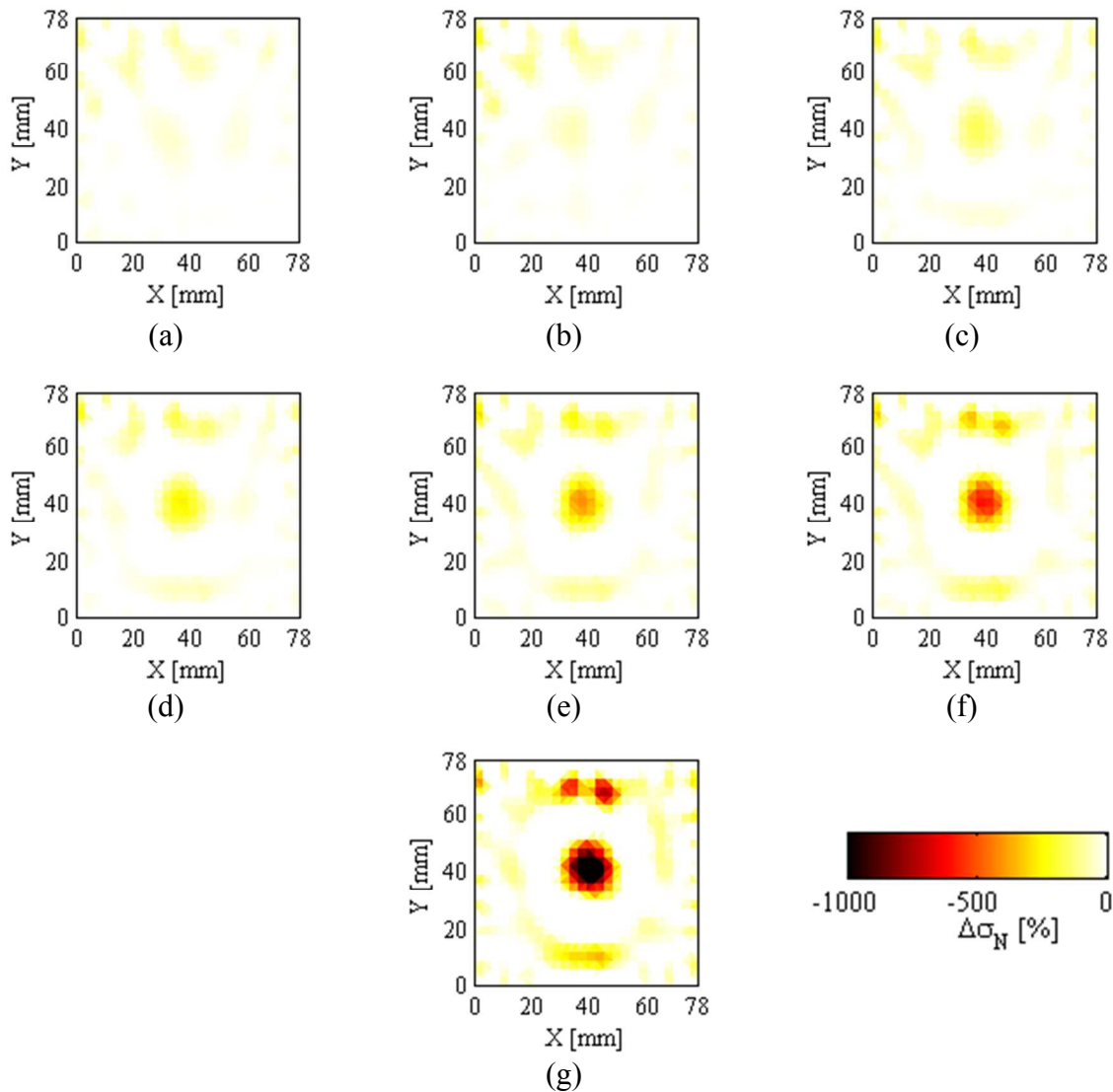
Figure 11. The spatial conductivity maps for drilled holes with diameters of (a) 1.59 mm, (b) 3.18 mm, (c) 4.76 mm, (d) 6.35 mm, (e) 7.94 mm, (f) 9.53 mm, and (g) 12.7 mm are shown.

observed in the results shown in Figure 11 is due to the anisotropic model. The degree of anisotropy might be higher than that measured using the resistance measurements. Nevertheless, the algorithm has successfully indicated the location and relative severity of enlarging damage from drilling.

To quantify the response due to the drilled holes, a metric (Σ_N) based on integrating the normalized EIT spatial conductivity response has been defined as:
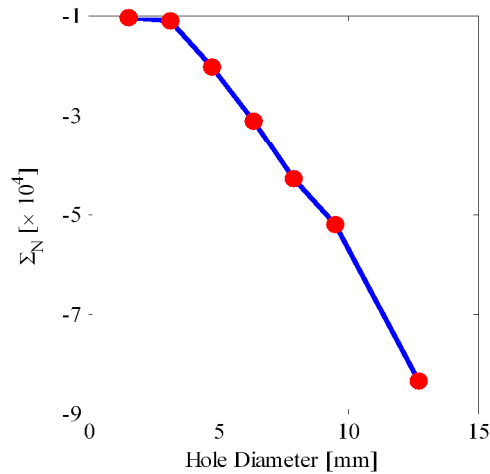
Figure 12. The calculated response metric Σ_N from EIT conductivity maps is plotted as a function of drilled center hole diameter.

$$\Sigma_N = \int_\Omega \sigma_N dA \quad \text{for} : \sigma_N < 0 \tag{10}$$

This integral in Equation (10) is performed over a subset of the sensing area $\boldsymbol{\Omega}$, which consists of only elements with negative values of σ_N (*i.e.*, due to damage). In this case, $\boldsymbol{\Omega}$ is a 30×30 mm^2 square region in the center of the sensing area. Σ_N has been calculated for each of the EIT spatial conductivity maps corresponding to the different drill-hole diameters. The resulting values for Σ_N are plotted as a function of hole diameter, as shown in Figure 12. A distinct linear trend between Σ_N and hole diameters from 3.18 mm to 12.7 mm is observable. This linearity not only indicates the smallest damage the algorithm can detect (*e.g.*, 3.18 mm relative to a 78 mm sensing area), but it also validates the use of a linear EIT reconstruction algorithm. The smallest detectable contrast is a function of the number of independent differential voltage measurements, or 448 in this case, and it given by [55]:

$$\mathrm{Re}s = \frac{1}{\sqrt{Meas_{Ind}}} \times 100\% = \frac{1}{\sqrt{448}} \times 100\% = 4.72\% \tag{11}$$

From Equation (11), the commonly accepted resolution of this approach is consistent with that determined by measurement. Furthermore, the center of the sensing region has the lowest sensitivity due to the distance from the electrodes [45], so smaller-sized damage may be detectable if they are located closer to the film boundaries.

In addition to characterizing EIT response to damage size, the method has also been tested for its sensitivity to the location of damage. The EIT reconstruction has been performed for each set of measurements corresponding to each drilled hole, as have been explained in Section 3.4. The results are presented in Figure 13. Figure 13a shows the EIT reconstruction for a 6.35 mm hole located in the center of the sensing area (*i.e.*, the first drilled hole). The reconstruction shows a localized change in spatial conductivity, although the results are elongated along the vertical direction. This effect is thought to be due to the anisotropic model, where the characterizing resistance measurements might not capture the correct anisotropic conditions. For the normalized spatial conductivity maps shown in Figures 13b to 13g, it can be seen that holes drilled in the top and bottom rows are clearly detected. However, Figures 13h and 13i show that damage corresponding to those locations can be detected, but the reconstruction pushes the localized changes in conductivity towards the center of the sensing area. Again, it is hypothesized that this is due to a discrepancy between the anisotropy of the conductivity distribution and that accounted for in the EIT reconstruction model. Despite these effects, when the corresponding response to each hole is characterized using the Σ_N metric, the response is fairly linear with respect to the number of holes present (Figure 14). It should be mentioned that the domain of integration, $\boldsymbol{\Omega}$ in this case, was set to the entire sensing area (due to the distribution of hole across the entire sensing area). The linearity of the response further validates that the linear MAP reconstruction approach is appropriate for these measurements.
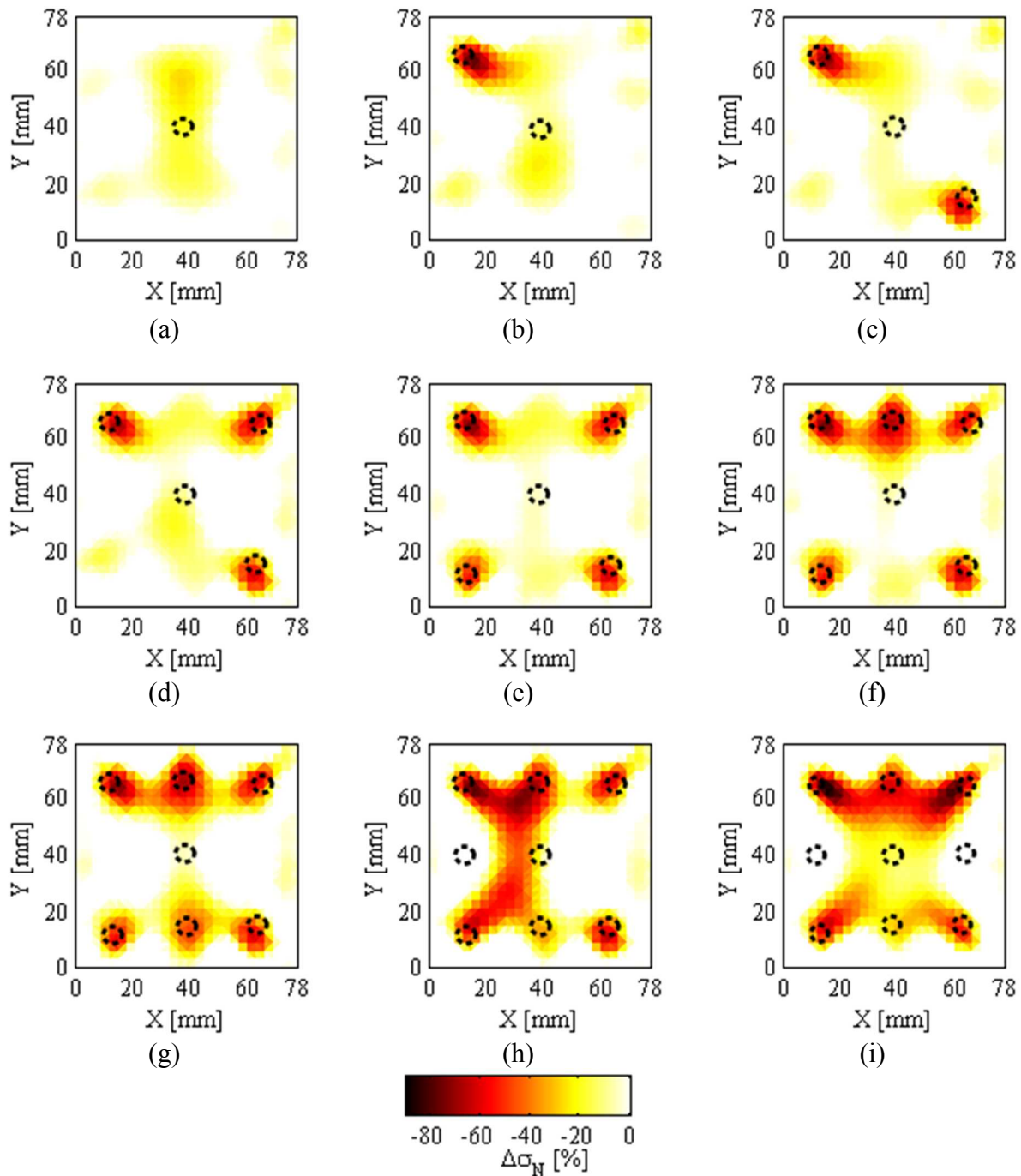
Figure 13. Normalized spatial conductivity maps for 6.35 mm holes drilled at different regions are shown. Each image corresponds to EIT measurements taken after a new hole has been created in the (a) center, (b) upper-left, (c) lower-right, (d) upper-right, (e) lower-left, (f) upper-center, (g) lower-center, (h) center-left, and (i) center-right of the 3×3 grid.
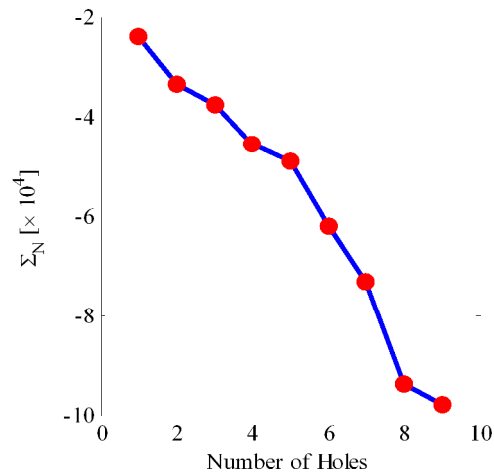
Figure 14. Σ_N has been calculated using EIT conductivity maps and plotted as a function of the number of drilled holes.

4.3 Impact Damage Detection

Section 4.2 has shown that the proposed film-enhanced composite specimens and EIT technique are able to detect and measure the location and severity of damage simulated by drilled holes (*i.e.*, full penetration of the MWCNT-PVDF film and composite specimen). However, damage due to impact is far more complex and does not always cause damage to the exterior plies. Thus, following the procedures in Section 3.5, a series of tests has been conducted for characterizing both the film and EIT's ability to detect impact damage. The experiment has been designed such that 20 J and 60 J of incident impact energy do not impart fracture damage to the exterior plies, and damage is confined within the internal structure of the multilayered GFRPs.

Figures 15a and 15c show two representative specimens impacted at 20 J and 60 J of nominal impact energy, and they do not cause apparent visual damage. Unlike visual inspection, EIT provides greater sensitivity to damage and can provide information regarding damage occurring internal to the material. The corresponding EIT spatial conductivity maps for specimens subjected to 20 J and 60 J of impact are shown in Figures 15b and 15d, respectively. It can be observed from these figures that the MWCNT-PVDF film and EIT method successfully
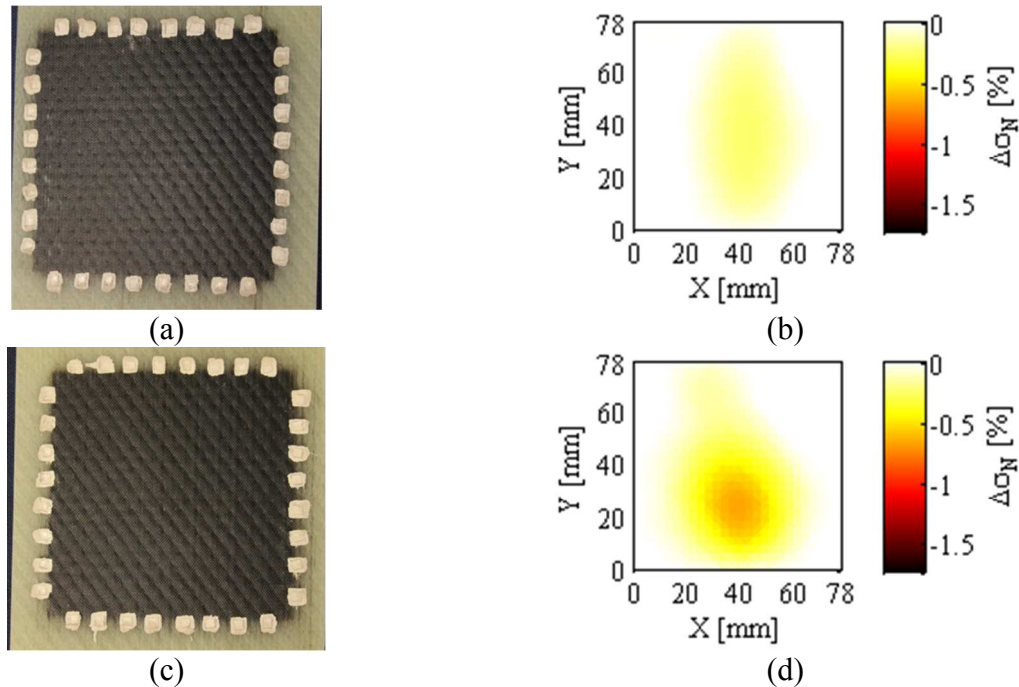
Figure 15. GFRP specimens have been subjected to low velocity impact testing. (a) The photograph and (b) EIT reconstruction of a specimen subjected to 20 J of impact is shown. (c) The photograph and (d) EIT map of a specimen subjected to 60 J of impact is also shown. The results suggest that EIT can detect the location and differences in magnitude of impact damage when it is not visible from the surface.

captures changes occurring internal to the structure. In addition, the normalized conductivity change for the 60 J impact case (Figure 15d) is more significant than the 20 J case (Figure 15b), which is as expected due to higher magnitudes of plastic deformation. The top films are not discussed here, because the conductivity change is negligible, which is consistent with other studies [58]. If this had been a composite aircraft wing, this damage would likely be invisible to the naked eye, remaining undetected for long periods of time and growing to critical levels.

For the 100 J impact energy case, Figure 16a clearly shows signs of visible damage to the outermost layer of the GFRP. This severe damage has also been effectively captured by EIT, as can be seen from the EIT reconstruction shown in Figure 16b. Furthermore, the specimen that has been subjected to 140 J of impact energy also shows the same type of severe surface damage as shown in Figure 16c. Once again, impact damage is successfully captured by the EIT
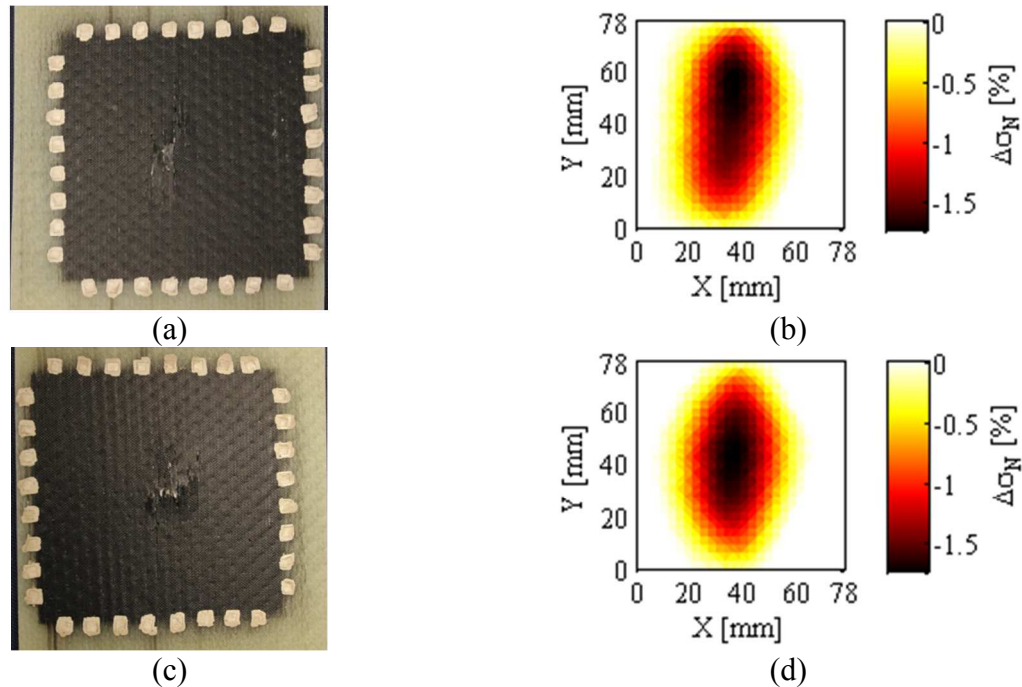
(a)

(b)

(c)

(d)

Figure 16. GFRP specimens have been subjected to impact testing. (a) The photograph and (b) EIT reconstruction of a specimen subjected to 100 J of impact is shown. (c) The photograph and (d) EIT map of a specimen subjected to 140 J of impact is also shown.

reconstruction of the MWCNT-PVDF film, as can be seen from Figure 16d. Significant decreases are observed in normalized conductivity near the vicinity of impact damage. It should be noted that the fracture in the center of the bottom face seems to elicit a spatial conductivity response that is elongated in the vertical direction. This is consistent with the response due to a 6.35 mm hole drilled in the center, as shown in Figure 13a.

To quantify the EIT reconstruction results to the various impact events, the Σ_N metric is once again implemented. This time, Ω is specified to be the entire sensing area due to the fact that the damaged area is likely to extend beyond the area of impact. The cumulative results are presented as an average (mean) of the responses from each level of impact energy, which is shown in Figure 17. The error bars are calculated as the standard error of the mean. Figure 17 shows that the damage metric becomes more negative as impact energy has increased from 20 J and 60 J. On the other hand, a sudden increase in the amount of damage has been observed after
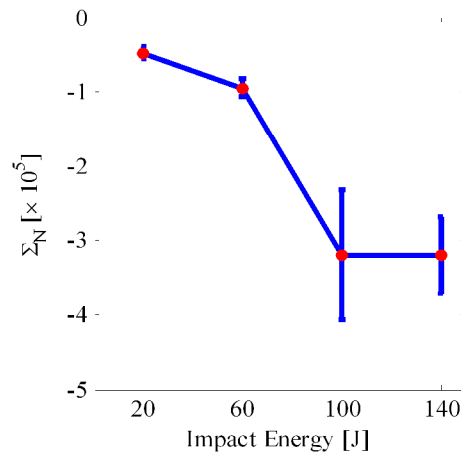
Figure 17. The response of the EIT images of embedded MWCNT-PVDF films to increasing damage due to impact on several specimens, as indicated by the Σ_N metric.

the 100 J of impact (and similarly for the 140 J case). This result is expected since a large change in conductivity occurs due to localized fracture, which has already been observed in Figures 16a and 16c. Since fracture is present in both of the 100 J and 140 J cases, it is not surprising that they exhibit roughly the same amount of damage (*i.e.*, as have been quantified using the damage metric Σ_N). From these results, it has been demonstrated that EIT spatial conductivity mapping of embedded MWCNT-PVDF films is able to detect, locate, and determine the severity of damage induced by impact upon GFRP composites.

5. Conclusions

This study serves as a step toward introducing EIT as a next-generation structural health monitoring methodology that can be used in conjunction with MWCNT-PVDF films for embedded damage detection. First, a strain sensitive MWCNT-PVDF film assembled using spray fabrication was discussed. The fabrication methodology was scalable and therefore appropriate for deployment onto large structures, while still maintaining sensitivity to smaller-scale damage mechanisms. Second, an electrical impedance tomography (EIT) differential spatial conductivity mapping algorithm was proposed and implemented. The conductivity

distribution of the spray-deposited sensor on unidirectional glass mats was found to be anisotropic in nature. Thus, the conductivity anisotropy was incorporated into the one-step linear MAP reconstruction algorithm as part of EIT. Then, the EIT algorithm was characterized for its resolution and sensitivity to well-defined damage induced from a drilling operation with a systematic variation in hole diameter and location. Additional validation studies were also conducted to verify the ability of the algorithm to detect various levels of low velocity impact damage on GFRP composites. Although more development is necessary prior to implementation of EIT for specific applications, the work presented here has shown the potential value that EIT offers for structural health monitoring applications.

Acknowledgements

References:

[1] Federal Highway Administration (FHWA) (2004). National Bridge Inspection Standards, Federal Highway Administration, Washington, DC.

[2] Nakagawara, V.B., Montgomery, R.W., Wood, G.W. and Nichols, J.J. (2003). A Demographic Profile of Nondestructive Inspection and Testing (NDI/NDT) Personnel: A Preliminary Report, Federal Aviation Administration, Washington, DC, USA.

[3] Hautamaki, C., Zurn, S., Mantell, S.C. and Polla, D.L. (1999). Experimental evaluation of MEMS strain sensors embedded in composites, Microelectromechanical Systems, Journal of, 8(3): 272-279.

[4] Kesavan, A., John, S. and Herszberg, I. (2008). Strain-based Structural Health Monitoring of Complex Composite Structures, Structural Health Monitoring, 7(3): 203-213.

[5] Cusano, A., Capoluongo, P., Campopiano, S., Cutolo, A., Giordano, M., Felli, F., Paolozzi, A. and Caponero, M. (2006). Experimental modal analysis of an aircraft model wing by embedded fiber Bragg grating sensors, Sensors Journal, IEEE, 6(1): 67-77.

[6] Tsutsui, H., Kawamata, A., Sanda, T. and Takeda, N. (2004). Detection of impact damage of stiffened composite panels using embedded small-diameter optical fibers, Smart Materials & Structures, 13(6): 1284-1290.

[7] Xinlong, C., Xiangyong, H., Jianghua, H. and Jinjun, L. (2008). Experimental Research on Embedded Fiber Bragg Grating Sensors Network for Solid Rocket Motors Health Monitor, First International Conference on Intelligent Networks and Intelligent Systems, Wuhan, China.

[8] Guoliang Jiang, Dawood, M., Peters, K. and Rizkalla, S. (2010). Global and Local Fiber Optic Sensors for Health Monitoring of Civil Engineering Infrastructure Retrofit with FRP Materials, Structural Health Monitoring, 9(4): 309-322.

[9] Wenger, M.P., Blanas, P., Shuford, R.J. and Das-Gupta, D.K. (1996). Acoustic emission signal detection by ceramic/polymer composite piezoelectrets embedded in glass-epoxy laminates, Polymer Engineering & Science, 36(24): 2945-2954.

[10] Ciampa, F. and Meo, M. (2012). Impact detection in anisotropic materials using a time reversal approach, Structural Health Monitoring, 11(1): 43-49.

[11] Tang, H.-Y., Winkelmann, C., Lestari, W. and La Saponara, V. (2011). Composite Structural Health Monitoring Through Use of Embedded PZT Sensors, Journal of Intelligent Material Systems and Structures, 22(8): 739-755.

[12] Giurgiutiu, V. and Zagrai, A. (2005). Damage Detection in Thin Plates and Aerospace Structures with the Electro-Mechanical Impedance Method, Structural Health Monitoring, 4(2): 99-118.

[13] Aymerich, F. and Staszewski, W.J. (2010). Experimental Study of Impact-Damage Detection in Composite Laminates using a Cross-Modulation Vibro-Acoustic Technique, Structural Health Monitoring, 9(6): 541-553.

[14] Winkelmann, C., Tang, H.-Y. and La Saponara, V. (2008). Influence of Embedded Structural Health Monitoring Sensors on the Mechanical Performance of Glass/Epoxy Composites, SAMPE 2008, Long Beach, CA, USA.

[15] Taya, M., Kim, W. and Ono, K. (1998). Piezoresistivity of a short fiber/elastomer matrix composite, Mechanics of materials, 28(1-4): 53-59.

[16] Todoroki, A. and Yoshida, J. (2004). Electrical Resistance Change of Unidirectional CFRP Due to Applied Load, JSME International Journal Series A Solid Mechanics and Material Engineering, 47(3): 357-364.

[17] Wang, S. and Chung, D. (2000). Piezoresistivity in continuous carbon fiber polymer-matrix composite, Polymer Composites, 21(1): 13-19.

[18] Wang, S. and Chung, D. (2007). Negative piezoresistivity in continuous carbon fiber epoxy-matrix composite, Journal of Materials Science, 42(13): 4987-4995.

[19] Inoue, H. and Ogi, K. (2007). Piezoresistance Behaviour of CFRP Cross-Ply Laminates with Transverse Cracking, Key Engineering Materials, 334(2): 961.

[20] Ogi, K. (2007). A Model for Piezoresistance Behavior in a CFRP Cross-Ply Laminate with Transverse Cracking, Journal of Solid Mechanics and Materials Engineering, 1(8): 975-985.

[21] Wang, S. and Chung, D.D.L. (2006). Self-sensing of flexural strain and damage in carbon fiber polymer-matrix composite by electrical resistance measurement, Carbon, 44(13): 2739-2751.

[22] Seo, D.-C. and Lee, J.-J. (1999). Damage detection of CFRP laminates using electrical resistance measurement and neural network, Composite Structures, 47(1–4): 525-530.

[23] Todoroki, A., Tanaka, M. and Shimamura, Y. (2005). Electrical resistance change method for monitoring delaminations of CFRP laminates: effect of spacing between electrodes, Composites Science and Technology, 65(1): 37-46.

[24] Minot, E.D., Yaish, Y., Sazonova, V., Park, J.-Y., Brink, M. and McEuen, P.L. (2003). Tuning Carbon Nanotube Band Gaps with Strain, Physical review letters, 90(15): 156401.

[25] Peng, S., O'Keeffe, J., Wei, C., Cho, K., Kong, J., Chen, R., Franklin, N. and Dai, H. (2001). Carbon nanotube chemical and mechanical sensors, 3rd International Workshop on Structural Health Monitoring, Stanford, CA, USA.

[26] Tombler, T.W., Zhou, C., Alexseyev, L., Kong, J., Dai, H., Liu, L., Jayanthi, C., Tang, M. and Wu, S.Y. (2000). Reversible electromechanical characteristics of carbon nanotubes under local-probe manipulation, Nature, 405(6788): 769-772.

[27] Gojny, F.H. and Schulte, K. (2004). Functionalisation effect on the thermo-mechanical behaviour of multi-wall carbon nanotube/epoxy-composites, Composites Science and Technology, 64(15): 2303-2308.

[28] Ma, P.C., Kim, J.K. and Tang, B.Z. (2007). Effects of silane functionalization on the properties of carbon nanotube/epoxy nanocomposites, Composites Science and Technology, 67(14): 2965-2972.

[29] Martin, C., Sandler, J., Shaffer, M., Schwarz, M.K., Bauhofer, W., Schulte, K. and Windle, A. (2004). Formation of percolating networks in multi-wall carbon-nanotube–epoxy composites, Composites Science and Technology, 64(15): 2309-2316.

[30] Sandler, J., Kirk, J., Kinloch, I., Shaffer, M. and Windle, A. (2003). Ultra-low electrical percolation threshold in carbon-nanotube-epoxy composites, Polymer, 44(19): 5893-5899.

[31] Wichmann, M.H.G., Sumfleth, J., Fiedler, B., Gojny, F. and Schulte, K. (2006). Multiwall carbon nanotube/epoxy composites produced by a masterbatch process, Mechanics of Composite Materials, 42(5): 395-406.

[32] Yaping, Z., Aibo, Z., Qinghua, C., Jiaoxia, Z. and Rongchang, N. (2006). Functionalized effect on carbon nanotube/epoxy nano-composites, Materials Science and Engineering: A, 435(145-149.

[33] Thostenson, E.T. and Chou, T.W. (2006). Carbon nanotube networks: sensing of distributed strain and damage for life prediction and self healing, Advanced Materials, 18(21): 2837-2841.

[34] Böger, L., Wichmann, M., Meyer, L. and Schulte, K. (2008). Load and health monitoring in glass fibre reinforced composites with an electrically conductive nanocomposite epoxy matrix, Composites Science and Technology, 68(7-8): 1886-1894.

[35] Thostenson, E.T. and Chou, T.-W. (2008). Real-time in situ sensing of damage evolution in advanced fiber composites using carbon nanotube networks, Nanotechnology, 19(21): 215713.

[36] Alexopoulos, N.D., Bartholome, C., Poulin, P. and Marioli-Riga, Z. (2010). Structural health monitoring of glass fiber reinforced composites using embedded carbon nanotube (CNT) fibers, Composites Science and Technology, 70(2): 260-271.

[37] Loyola, B.R., La Saponara, V. and Loh, K.J. (2010). In Situ Strain Monitoring of Fiber-Reinforced Polymers using Embedded Piezoresistive Nanocomposites, Journal of Material Science, 45(24): 6786-6798.

[38] Calderon, A.P. (2006). On an inverse boundary value problem, Comp. Appl. Math, 25(2-3): 133-138.

[39] Cheney, M., Isaacson, D., Newell, J., Simske, S. and Goble, J. (1990). NOSER: An algorithm for solving the inverse conductivity problem, International Journal of Imaging Systems and Technology, 2(2): 66-75.

[40] Adler, A. and Guardo, R. (1996). Electrical impedance tomography: regularized imaging and contrast detection, IEEE Transactions on Medical Imaging, 15(2): 170-179.

[41] Yorkey, T.J., Webster, J.G. and Tompkins, W.J. (1987). Comparing reconstruction algorithms for electrical impedance tomography, IEEE Transactions on Biomedical Engineering, 11): 843-852.

[42] Hua, P., Woo, E.J., Webster, J.G. and Tompkins, W.J. (1991). Iterative reconstruction methods using regularization and optimal current patterns in electrical impedance tomography, IEEE Transactions on Medical Imaging, 10(4): 621-628.

[43] Polydorides, N., Lionheart, W.R.B. and McCann, H. (2002). Krylov subspace iterative techniques: on the detection of brain activity with electrical impedance tomography, IEEE Transactions on Medical Imaging, 21(6): 596-603.

[44] Vauhkonen, M. (1997), Electrical impedance tomography and prior information. Dissertation, University of Kuopio, University of Kuopio.

[45] Polydorides, N. (2002), Image Reconstruction Algorithms For Soft-Field Tomography. Doctoral Dissertation, University of Manchester Institute of Science and Technology, Manchester, United Kingdom.

[46] Abdellatif El, B. (2005). Inverse source problem in an anisotropic medium by boundary measurements, Inverse Problems, 21(5): 1487.

[47] Abascal, J.F.P.J., Arridge, S.R., Atkinson, D., Horesh, R., Fabrizi, L., De Lucia, M., Horesh, L., Bayford, R.H. and Holder, D.S. (2008). Use of anisotropic modelling in electrical impedance tomography; Description of method and preliminary assessment of utility in imaging brain function in the adult human head, Neuroimage, 43(2): 258-268.

[48] Loh, K.J., Hou, T.C., Lynch, J.P. and Kotov, N.A. (2009). Carbon Nanotube Sensing Skins for Spatial Strain and Impact Damage Identification, Journal of Nondestructive Evaluation, 28(1): 9-25.

[49] Hou, T., Loh, K. and Lynch, J. (2007). Spatial conductivity mapping of carbon nanotube composite thin films by electrical impedance tomography for sensing applications, Nanotechnology, 18(31): 315501.

[50] Pyo, S., Loh, K.J., Hou, T.C., Jarva, E. and Lynch, J.P. (2011). A wireless impedance analyzer for automated tomographic mapping of a nanoengineered sensing skin, Smart Structures and Systems, 8(1): 139-155.

[51] Lazarovitch, R., Rittel, D. and Bucher, I. (2002). Experimental crack identification using electrical impedance tomography, NDT and E International, 35(5): 301-16.

[52] Alirezaei, H., Nagakubo, A. and Kuniyoshi, Y. (2007). A highly stretchable tactile distribution sensor for smooth surfaced humanoids, 7th IEEE-RAS International Conference on Humanoid Robots, Pittsburgh, Pennsylvania, USA.

[53] Alirezaei, H., Nagakubo, A. and Kuniyoshi, Y. (2009). A tactile distribution sensor which enables stable measurement under high and dynamic stretch, IEEE Symposium on 3D User Interfaces, Lafayette, Louisiana, USA.

[54] Paulson, K., Breckon, W. and Pidcock, M. (1992). Electrode modelling in electrical impedance tomography, SIAM Journal on Applied Mathematics, 1012-1022.

[55] Graham, B. and Adler, A. (2006). Objective selection of hyperparameter for EIT, Physiological measurement, 27(S65):

[56] O'Connell, M.J., Boul, P., Ericson, L.M., Huffman, C., Wang, Y., Haroz, E., Kuper, C., Tour, J., Ausman, K.D. and Smalley, R.E. (2001). Reversible water-solubilization of single-walled carbon nanotubes by polymer wrapping, Chemical Physics Letters, 342(3): 265-271.

[57] Mazov, I., Kuznetsov, V., Moseenkov, S., Ishchenko, A., Romanenko, A., Anikeeva, O., Buryakov, T., Korovin, E.Y., Zhuravlev, V. and Suslyaev, V. (2010). Electrophysical and Electromagnetic Properties of Pure MWNTs and MWNT/PMMA Composite Materials Depending on Their Structure, Fullerenes, Nanotubes, and Carbon Nanostructures, 18(4-6): 505-515.

[58] Shyr, T.-W. and Pan, Y.-H. (2003). Impact resistance and damage characteristics of composite laminates, Composite Structures, 62(2): 193-203.